Nanoscale

PAPER

View Article Online
View Journal | View Issue

Cite this: *Nanoscale*, 2025, **17**, 5858

Laser-assisted thermoelectric-enhanced hydrogen peroxide biosensors based on Ag_2Se nanofilms for sensitive detection of bacterial pathogens†

Huangshui Ma,‡[a,g] Shiyu Pu,‡[b] Shiyu Jia,[a] Shengduo Xu,[c] Qiwei Yu,[d] Lei Yang,*[e] Hao Wu*[f] and Qiang Sun*[a,g]

Thermoelectric (TE) materials can convert the heat produced during biochemical reactions into electrical signals, enabling the self-powered detection of biomarkers. In this work, we design and fabricate a simple Ag_2Se nanofilm-based TE biosensor to precisely quantify hydrogen peroxide (H_2O_2) levels in liquid samples. A chemical reaction involving horseradish peroxidase, ABTS and H_2O_2 in the specimens produces a photothermal agent—ABTS (2,2′-azino-bis(3-ethylbenzothiazoline-6-sulfonic acid)) free radical, which triggers the heat fluctuations at the TE sensor through the photo-thermal effect, eventually enabling the sensing of H_2O_2. Consequently, the constructed sensor can achieve a detection limit of 0.26 μM by a three-leg TE device design. Further investigations suggest that the application of our TE sensor can be extended in testing H_2O_2 in beverages (including milk, soda water, and lemonade) and evaluating the load of bacterial pathogens relevant to dental diseases and infections including *Streptococcus sanguinis* and *Methicillin-resistant Staphylococcus aureus* with high analytical accuracy. This strategy utilizes the combination of high thermoelectric performance with chemical reactions to realize a straightforward and accurate biomarker detection method, making it suitable for applications in medical diagnostics, personalized health monitoring, and the food industry.

Received 19th November 2024,
Accepted 30th January 2025

DOI: 10.1039/d4nr04860a

rsc.li/nanoscale

1. Introduction

Quantifying biological markers that offer valuable insights into physiological function is essential for early disease diagnosis, healthcare monitoring, and developing novel pharmaceuticals.[1–3] The energetic dynamics characterized by absorption and release during biochemical reactions presents a tangible target for detecting these biomarkers.[4] Thermoelectric (TE) materials and devices, utilizing the Seebeck effect, can convert thermal energy into an electrical voltage without the requirement of external power,[5–9] which enables the conversion of thermal variations linked to biological activities into detectable electrical signals, facilitating the monitoring of heat-dependent processes within biological systems.[10–13] The recent rapid advancement of TE materials with high room-temperature performance, such as those reported in Ag_2Se,[14–17] Bi_2Te_3,[18] Cu_2Se,[19] and $Mg_3(Sb, Bi)_2$-based derivatives,[20] has established a robust material foundation for precise thermal detection, which holds significant promise for enhancing clinical diagnostics and health monitoring applications.[21]

Hydrogen peroxide (H_2O_2), as a key member of reactive oxygen species (ROS), is a pivotal molecule in various biological scenarios, detectable in infected wounds,[22] inflammatory conditions,[23] and a broad spectrum of food products.[24] Concentrations of H_2O_2 that exceed certain thresholds are potentially dangerous, particularly upon ingestion or inhalation.[25] Notably, the concentration of H_2O_2 can act as an indicator of bacterial load associated with particular diseases. For example, *Streptococcus sanguinis* (*S. sanguinis*) releases H_2O_2,[22,26] while methicillin-resistant *Staphylococcus aureus* (*MRSA*) secretes catalase to decompose H_2O_2.[27,28] Thus, monitoring the concentration of H_2O_2 in biological samples can serve as a valuable approach for clinical diagnosis, particularly in the context of infectious diseases.[29] Current methods for

[a]*State Key Laboratory of Oral Diseases, National Center for Stomatology, National Clinical Research Center for Oral Diseases, West China Hospital of Stomatology, Sichuan University, Chengdu 610041, China. E-mail: qiangsun@scu.edu.cn*
[b]*Department of Ultrasonography, West China Second University Hospital, Sichuan University, Chengdu 610041, China*
[c]*Institute of Science and Technology Austria, Klosterneuburg 3400, Austria*
[d]*The First Clinical College, Changsha Medical University, Changsha 410005, China*
[e]*College of Materials Science and Engineering, Sichuan University, Chengdu 610065, China. E-mail: lyang1986@scu.edu.cn*
[f]*Department of Stomatology, The First Medical Centre, Chinese PLA General Hospital, Beijing 100039, China. E-mail: wh_dds@126.com*
[g]*Sichuan Provincial Engineering Research Center of Oral Biomaterials, Chengdu 610064, China. E-mail: qiangsun@scu.edu.cn*

†Electronic supplementary information (ESI) available. See DOI: https://doi.org/10.1039/d4nr04860a

‡These authors contributed equally to this work.

H_2O_2 detection encompass techniques that include high-performance liquid chromatography,[30] chemiluminescence,[31] electrochemical,[32] and fluorescence-based assays.[33,34] Nevertheless, these methods face challenges such as high costs, time-consuming procedures, and complex operations,[35] which calls for the creation of more portable and simple biosensing tools.

In this work, due to the high TE performance at room temperatures,[14,36,37] superior biocompatibility,[38] and simplicity of synthetic films,[11] Ag_2Se nanofilms were fabricated on light-curable three-dimensional (3D) printing resin substrates to prepare TE biosensors, which serve as a sensory component of the device. In this device design, the energy changes were detected with respect to the quantity of the H_2O_2 concentration. This process is driven by the heat generated when a laser irradiates the photothermal agent, the 2,2′-azino-bis(3-ethylbenzothiazoline-6-sulfonic acid) (ABTS) oxidative product, which is oxidized by H_2O_2 and horseradish peroxidase (HRP). This enables remarkable sensitivity detection of the concentration of H_2O_2, with a detection limit of 0.26 μM in standard solution testing and 0.58 μM in beverage testing, surpassing the maximum permissible limit of the standard set by the FDA[39,40] for H_2O_2 content in food products. Furthermore, its ability to detect bacteria has also been confirmed in this work. The detection limit for bacteria such as *S. sanguinis* and *MRSA* can reach as low as 3×10^4 CFU ml^{-1} by precisely measuring the concentration of H_2O_2, fulfilling the clinical diagnostic requirements for infected wounds (10^5 CFU ml^{-1}),[41] thereby offering a novel alternative method for the diagnosis and monitoring of infectious diseases such as dental caries, periodontitis, and drug-resistant bacterial infection. In summary, this TE-based sensory approach utilizing the photothermal–electric conversion potentially paves a new way for advancements in medical diagnostics, food quality examination, and personalized healthcare monitoring, which can contribute to the development of innovative biomedical tools aimed at enhancing our understanding of the intricate thermal dynamics within biological activities.

2. Results and discussion

2.1. Architecture of the Ag_2Se-based H_2O_2 biosensor

Fig. 1 illustrates the principles, architecture, and applications of the Ag_2Se-based biosensor. The underlying mechanism of the biosensor is depicted in Fig. 1a. When HRP is present, H_2O_2 can oxidize ABTS to produce ABTS free radical ($ABTS^{\bullet+}$). When excited by infrared light, $ABTS^{\bullet+}$ releases heat, creating a temperature gradient across the biosensor, which in turn generates a voltage signal through the Seebeck effect. The Ag_2Se-based biosensor's voltage output is governed by the temperature gradient it generates, which is directly influenced by the quantity of $ABTS^{\bullet+}$ produced. Consequently, the voltage signal emitted by the Ag_2Se-based sensor serves as a reliable indicator for quantifying the concentration of H_2O_2 in the sample. Then Fig. 1b–d illustrates the detailed fabrication and working mechanism of the Ag_2Se-based biosensor based on an Ag_2Se TE film. The standard solution, which contains HRP and ABTS (see Fig. 1f), was mixed with solutions containing different concentrations of H_2O_2 and then added to the cavity of the biosensor on one side. Afterward, the laser beam is directed perpendicularly onto the solution, where the photothermal conversion of $ABTS^{\bullet+}$ induces a temperature elevation within the solution, resulting in a temperature differential across the biosensor's opposing sides. The induced thermal gradient across the Ag_2Se-based biosensor results in a voltage output *via* the Seebeck effect within the Ag_2Se sensing layer, which is directly proportional to the concentration of H_2O_2 being measured. Based on the above working mechanism, Fig. 1e–g illustrates three specific applications of the TE biosensor principle in detecting H_2O_2, which involves assessing the H_2O_2 concentration in food samples and quantifying the bacterial loads of *S. sanguinis* as well as *MRSA*. The respective findings for these applications will be presented in Fig. 3–5. This study constitutes the first report on the fabrication of TE films using commercially available 3D-printed light-curing resin, enabling the rapid prototyping and fabrication of TE devices with complex geometries.

2.2. Characterization of Ag_2Se films

To exhibit the morphological characteristics of the Ag_2Se nanofilms, Fig. 2a and b present scanning electron microscopy (SEM) images of Ag nanofilms and Ag_2Se nanofilms with different thicknesses. The SEM images captured from various perspectives of Ag_2Se films reveal the precise control over the thickness of the Ag film, facilitating the effective synthesis of Ag_2Se films with differential thicknesses after the selenization process (Fig. 2c). To clarify the crystal structure of the Ag_2Se film deposited on the resin substrate, room-temperature X-ray diffraction (XRD) analyses were conducted on Ag_2Se nanofilms of varying thicknesses from 200 to 600 nm, as depicted in Fig. 2d. The XRD diffraction patterns for all films were successfully indexed to the β-phase of Ag_2Se, in alignment with the standard PDF card for Ag_2Se (PDF no. 24-1041). Notably, no diffraction peak indicative of Ag impurities was detected. The obtained XRD patterns verified the polycrystalline nature of the Ag_2Se films, characterized by relatively intense (201) diffraction peaks, which correlates well with the SEM images. Additionally, the broad peaks preceding the Ag_2Se peaks in the XRD patterns are attributed to the organic resin serving as the substrate. To investigate the chemical composition of the synthesized Ag_2Se film in greater detail, X-ray photoelectron spectroscopy (XPS) was performed (refer to Fig. S1†). Fig. 2e and f present the XPS survey spectra and the associated high-resolution spectra for the 200 nm thick Ag_2Se film, respectively. These spectra exhibit clear peaks that correspond to the Ag $3d_{3/2}$, Ag $3d_{5/2}$, Se $3d_{3/2}$, and Se $3d_{5/2}$ orbitals, confirming the presence of Ag_2Se compounds. The absence of peaks attributable to elemental silver or elemental selenium in the XPS survey spectra suggests that the selenization reaction has proceeded to completion. To better understand the structure of the Ag_2Se film and the resin substrate, Fig. 2g displays a trans-

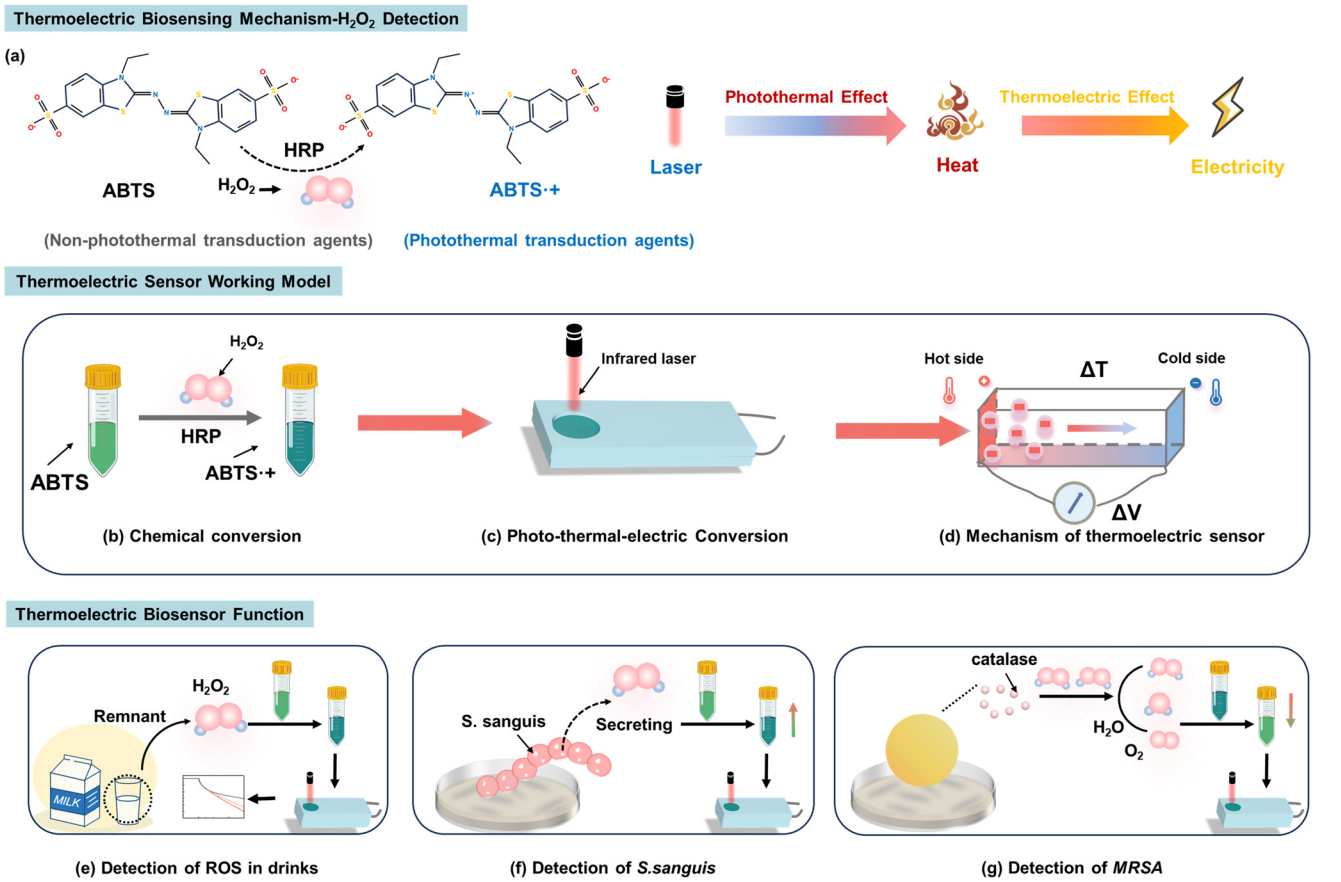

Fig. 1 Mechanism of the thermoelectric sensor. (a) The principles of the Ag_2Se-based TE biosensor. (b–d) The working mechanism of the TE biosensor, and (e and f) their application examples.

mission electron microscopy (TEM) image of a cross-section of the Ag_2Se film. This image clearly shows the detailed structure of the film. Fig. 2g also presents a high-resolution transmission electron microscopy (HRTEM) image of the interface between the Ag_2Se film and the resin substrate. This image reveals lattice fringes with a spacing of 0.24 nm, corresponding to the *d*-spacing of the (112) plane, which is consistent with previously reported high-performance Ag_2Se,[42] signifying a high level of crystallinity and definitively confirming the β-Ag_2Se crystal structure. Fig. 2h depicts the high-angle annular dark-field scanning transmission electron microscopy (HAADF-STEM) image of the Ag_2Se/resin interface. Complementarily, Fig. 2i offers an elemental mapping of silver (Ag) and selenium (Se) within the Ag_2Se sample. To validate the compositional concentrations of the synthesized Ag_2Se films, energy-dispersive X-ray spectroscopy (EDS) point analysis (Fig. S2†) was performed, which aligns with the theoretical stoichiometric ratio of Ag_2Se. Consequently, the synthesis method employed for the Ag_2Se is conducive to enhancing the material's performance characteristics.

Fig. 2j shows the voltage response of Ag_2Se films with differing thicknesses. Upon exposure to an object heated to a uniform temperature, Ag_2Se films of differing thicknesses demonstrated that the Ag_2Se film with 200 nm achieves a more rapid voltage increase. The results align with prior studies,[43] suggesting that the response time of thin films is inversely proportional to their thickness. This relationship is further elucidated by the heat transport response time, which is approximately $4l^2/\pi^2D$, where 'l' represents the thickness of the thermoelement and 'D' denotes the thermal diffusivity. Thereby, thinner films are more appropriate for the fabrication of sensitive biosensor devices. To understand the TE performance of obtained Ag_2Se films on resin substrates, Fig. 2k shows the Seebeck coefficient S, electrical conductivity σ, and power factor (PF) of Ag_2Se film with various temperatures at a thickness of 200 nm, the S and σ of the Ag_2Se films exhibit minimal variation within the temperature range from 295 to 330 K. As Fig. S3† displays, Ag_2Se nanofilms deposited on a resin substrate maintain a relatively stable TE performance regardless of the thickness, which is expected to ensure the stability of sensor performance. Fig. S4† shows that Ag_2Se films with different thicknesses exhibit consistent TE performance across various temperatures. Hence, given that the 200 nm-thick Ag_2Se film exhibits a quicker response time and consistent TE properties across different temperature ranges, it was chosen to fabricate the Ag_2Se-based biosensor. Additionally, after incu-

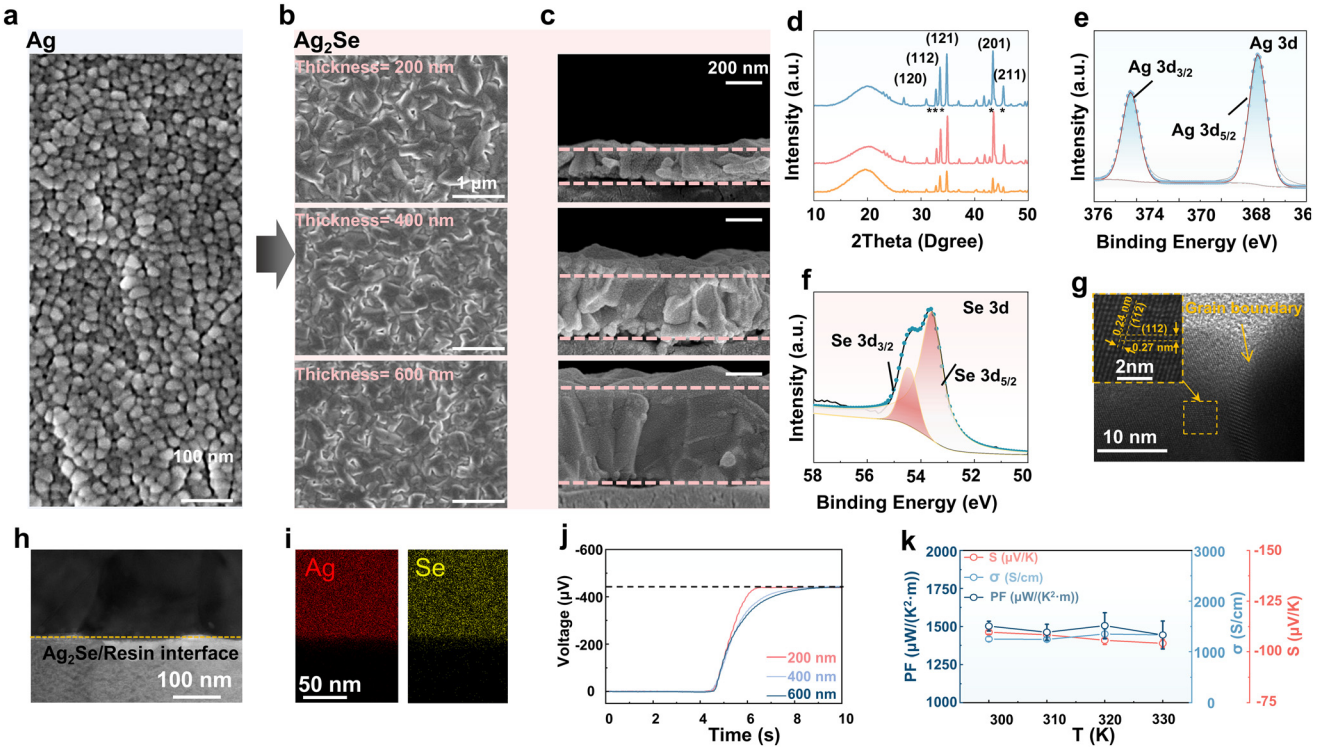

Fig. 2 (a) Top-view SEM images of the Ag films on the resin substrate. (b and c) Top-view and side-view SEM images of the Ag_2Se films on the resin substrate with various thicknesses. (d) XRD patterns of the Ag_2Se nanofilm with various thicknesses on resin substrates. (e and f) XPS spectrum of Ag_2Se, showing the high-resolution XPS spectrum of Ag 3d and Se 3d. (g) High-resolution TEM image of the cross-sectional area of the Ag_2Se film obtained on the resin substrate, with the inset implying the crystal structure of Ag_2Se. (h) STEM high-angle annular dark-field image of the Ag_2Se/resin interface. (i) Elemental distribution of Ag and Se in the Ag_2Se film. (j) Voltage response of Ag_2Se films with differing thicknesses, demonstrating the sensory response time when subjected to a heat source. (k) Temperature-dependent Seebeck coefficient S, electrical conductivity σ, and power factor (PF) of the Ag_2Se film with a thickness of 200 nm.

bating Ag_2Se films with human umbilical vein endothelial cells (HUVEC), the biocompatibility of the Ag_2Se thin films was confirmed by the CCK-8 assay. There was no significant change in cell viability compared to the normal group, due to its high stability in solution, Ag_2Se scarcely releases ions (Fig. S5†), indicating good biocompatibility[38] and suitability as a material for constructing biosensors.

2.3. Sensing performance of the Ag_2Se-based H_2O_2 biosensor

Fig. 3a illustrates the fabrication process of the Ag_2Se-based H_2O_2 sensor. Initially, an Ag film is deposited onto a 3D-printed resin block *via* ion sputtering (refer to Fig. S6†). The thickness and morphology of the Ag_2Se films are meticulously controlled by adjusting the sputtering duration and mask design. Subsequently, the deposited Ag films are subjected to treatment with a Na_2S/Se solution, facilitating the conversion to Ag_2Se through a selenization reaction. The resulting Ag_2Se films function as the sensory element, converting the heat produced from the laser-irradiated $ABTS^{\bullet+}$ solution into detectable signals. The encapsulating polyimide (PI) films serve to isolate the Ag_2Se from environmental humidity and inhibit oxidation by atmospheric oxygen, thereby providing both a protective barrier and an insulating layer for the sensor component.

Then the entire setup is supported and protected by a 3D-printed resin frame (Fig. S7†), ensuring both stability and durability for the Ag_2Se-based H_2O_2 biosensor. To help evaluate the performance of the Ag_2Se-based H_2O_2 biosensor, the standard solution of H_2O_2 with different concentrations was prepared by measuring UV-vis absorption spectrum values (Fig. 3b). The results showed that the standard solution displayed higher absorption intensity when oxidized by higher concentrations of H_2O_2 under 808 nm laser irradiation, following a linear relationship, (Fig. 3c). To confirm the specificity of this detection strategy, we conducted a comparative analysis (Fig. 3d) of the Ag_2Se-based biosensor's response to H_2O_2 and other common substances, including alcohol, glycine, glycerol, sodium chloride, and uric acid. The results indicated that the sensor exhibited a specific response only to H_2O_2.

The Ag_2Se-based biosensor's sensitivity to varying concentrations of H_2O_2 was then evaluated. As presented in Fig. 3e, the biosensor exhibited distinct voltage response curves corresponding to different H_2O_2 concentrations, demonstrating that higher concentrations elicited stronger voltage responses. Further analysis (Fig. 3f) of the voltage difference ΔV at the 60th second revealed a direct correlation between voltage difference and H_2O_2 concentration within a specific range,

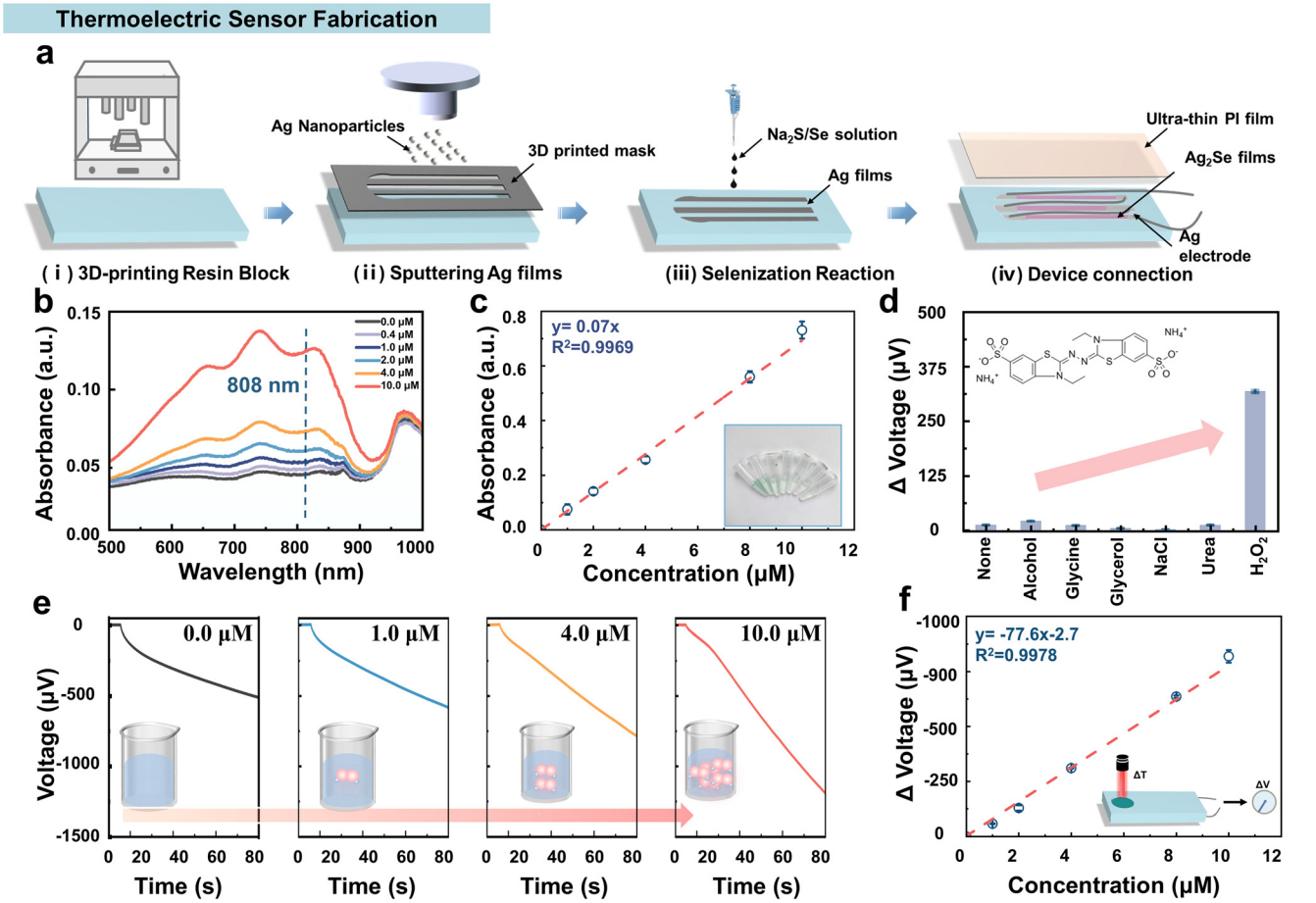

Fig. 3 (a) Fabrication process of the Ag_2Se-based biosensor, (b) UV-vis spectra of the standard solution under different concentrations of H_2O_2, and (c) relationships between 808 nm absorbance of the standard solution and H_2O_2 concentrations ranging from 0.0 μM to 10.0 μM. The inset shows the picture of the standard solution under different concentrations of H_2O_2. (d) The specificity of the sensor towards H_2O_2. (e) The voltage response curve of the biosensor with various concentrations of H_2O_2. (f) Relationship between voltage difference in 60 s with H_2O_2 concentrations ranging from 0.0 μM to 10.0 μM.

with an impressive precision of up to 77.6 μV μM^{-1}, which aligns well with the theoretical calculations presented in Fig. S8,† underscoring the biosensor's high accuracy and reliability. Moreover, based on the equation $3\sigma/S$ (σ representing the standard deviation of blank samples and S denoting the slope of the calibration curve), the detection limit was calculated at 0.26 μM. To assess the repeatability and stability of the sensor, continuous testing was conducted on the same concentration of H_2O_2 for 20 consecutive times, as well as over a period of seven days (Fig. S9†). The results showed no significant differences among the tests conducted at different times and days, confirming the excellent repeatability and stability of the sensor. This performance is attributed to the encapsulation of Ag_2Se by PI film, which effectively isolates it from the influence of air and water, ensuring the stability of its high-performance S. The stability of the sensor under different pH levels and ion concentrations has been verified (Fig. S10†), the results show that the sensor maintains good stability in a pH range of 5–9 and ion concentrations ranging from 0 to 8 M. Additionally, we compared our findings with recently reported studies on H_2O_2 sensors based on amperometry, electrochemical, or fluorescent detection techniques, revealing that our Ag_2Se-based biosensor is competitive in the current research landscape (Fig. S11, and Table S1†). Therefore, the Ag_2Se-based biosensor exhibits high sensitivity and specificity towards H_2O_2.

2.4. Detection of H_2O_2 in beverages

The extensive use of H_2O_2 in beverages and various food products for preservation and freshness enhancement calls for precisely controlling its concentration, as excessive H_2O_2 can pose significant health risks to humans,[44] and detecting H_2O_2 in beverages is critical to ensure product safety and quality for consumption.[45] In this study, we subjected a variety of beverages, including milk, soda, and lemonade, to controlled amounts of H_2O_2 to mimic different quality levels within the drinks. Subsequently, the treated beverage samples were evaluated using our Ag_2Se-based biosensors, with parallel analysis conducted using commercial reagent kits and a microplate reader as a comparative method. For example, the measure-

ment of H_2O_2 concentrations within milk samples using TE biosensors demonstrated a consistent increase in voltage response with escalating H_2O_2 concentrations (Fig. 4a), exhibiting a linear relationship between voltage differential and concentration (Fig. 4b). These findings concurred with those obtained through traditional reagent kit methods (Fig. 4c), validating the accuracy and reliability of the applied methodology. Then the performance of Ag_2Se-based TE biosensors in detecting the H_2O_2 concentration in soda water (Fig. 4d–f) and lemonade (Fig. 4g–i) was further examined. Consequently, according to the limit of detection (LOD) calculation formula, the LODs of H_2O_2 in milk, soda water, and lemonade tested by this sensor are 0.58, 0.71, and 0.72 μM, respectively, which are significantly lower than the FDA's permissible limit of 14.7 μM for H_2O_2 in food. Moreover, it exhibits an excellent linear relationship, making it a reliable method and tool for food monitoring. This biosensor significantly reduces the time required for the substrate incubation step in H_2O_2 testing, as compared to traditional kits, while also offering a more affordable option, enabling reuse, and maintaining comparable accuracy, thereby substantially expediting the detection of H_2O_2 in beverages and foods.

2.5. Ag_2Se-based biosensor-based detection of *S. sanguinis*

Dental caries is one of the most common diseases, which if not treated promptly can cause pain, abscess, and even destruction of the alveolar bone.[46,47] The growth of *S. sanguinis* is negatively correlated with dental caries, as it can

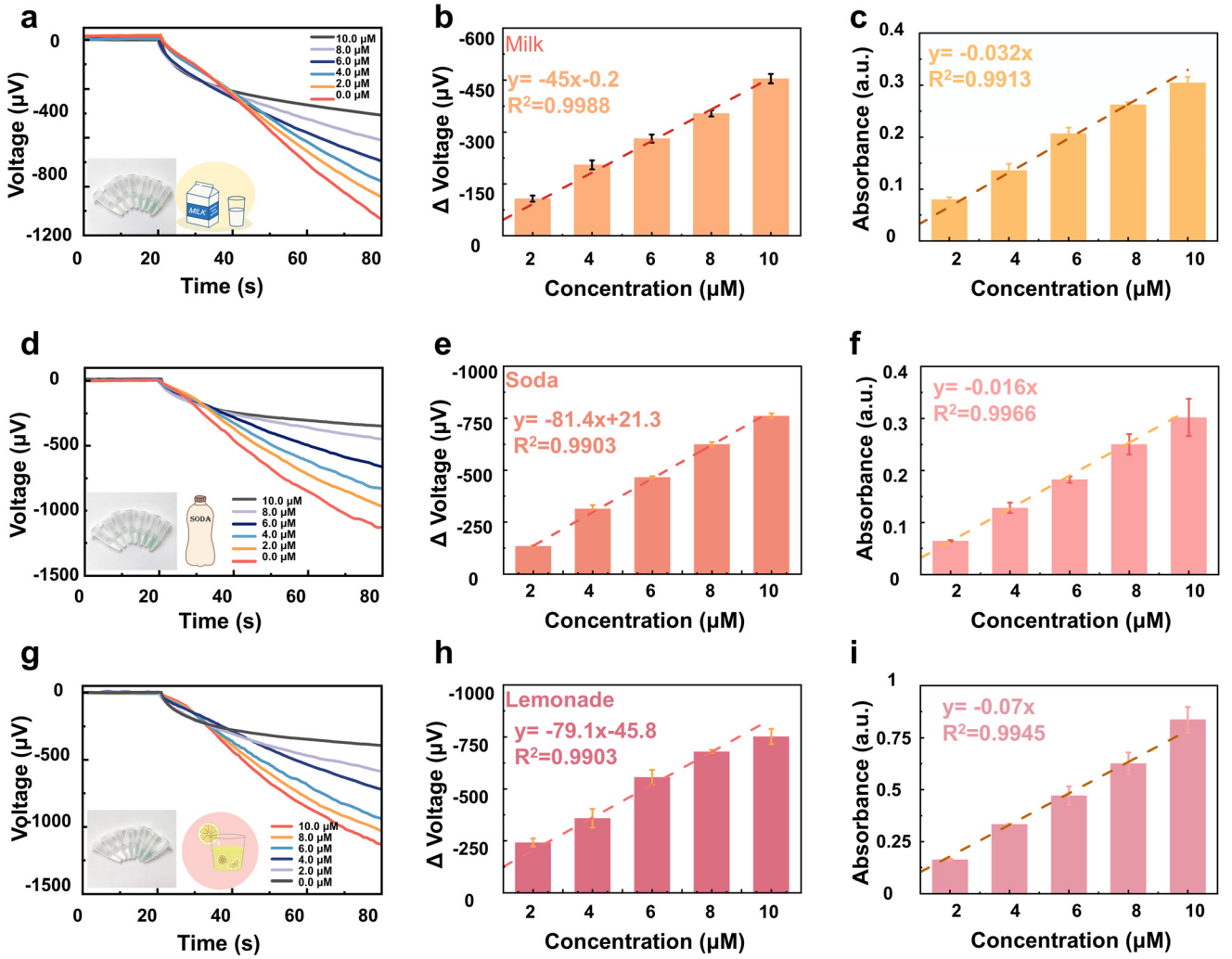

Fig. 4 (a) The voltage response curve of the biosensor with various concentrations of H_2O_2 in milk. The inset is the picture of the standard solution under different concentrations of H_2O_2. (b) Relationship between voltage difference in 60 s with H_2O_2 concentrations in milk. (c) The absorbance of various concentrations of H_2O_2 in milk with the colorimetric method. (d) The voltage response curve of the biosensor with various concentrations of H_2O_2 in soda water. The inset is the picture of the standard solution under different concentrations of H_2O_2. (e) Relationship between voltage difference in 60 s with H_2O_2 concentrations in soda water. (f) The absorbance of various concentrations of H_2O_2 in soda water using the colorimetric method. (g) The voltage response curve of the biosensor with various concentrations of H_2O_2 in lemon water. The inset is the picture of the standard solution under different concentrations of H_2O_2. (h) Relationship between voltage difference in 60 s with H_2O_2 concentrations in lemon water. (i) The absorbance of various concentrations of H_2O_2 in lemon water with colorimetric method.

secrete H_2O_2 to inhibit the growth of *Streptococcus mutans*, the most important cariogenic bacterium.[48,49] In addition to being an early colonizer in the oral cavity, it significantly contributes to the pathogenesis of infective endocarditis, a condition affecting the cardiac valves or endocardial lining, posing a complex challenge in clinical treatment.[50] Thus, the bacterial load of *S. sanguinis* bacteria is expected to be detected by the Ag_2Se-based biosensor due to their secretion of H_2O_2.

Fig. 5a demonstrates the operational steps and underlying principles for measuring the concentration of *S. sanguinis* using the Ag_2Se-based biosensor. First, the H_2O_2 secreted by *S. sanguinis* was incubated with the standard solution that contains HRP and ABTS to produce $ABTS^{\bullet+}$. Then when excited by an 808 nm laser, $ABTS^{\bullet+}$ releases heat causing a temperature difference in the sensor and generating a voltage signal. Fig. 5b, c and Fig. S12† confirm the classical morphology of *S. sanguinis* and its freedom from contamination with other bacteria together through microscopy and scanning electron microscopy imaging. Notably, the SEM image reveals the classical chain-like arrangement of *S. sanguinis*. After culturing with different concentrations of *S. sanguinis* (ranging from 2 to 10×10^5 CFU ml^{-1}) on the BHI agar medium for two days, the

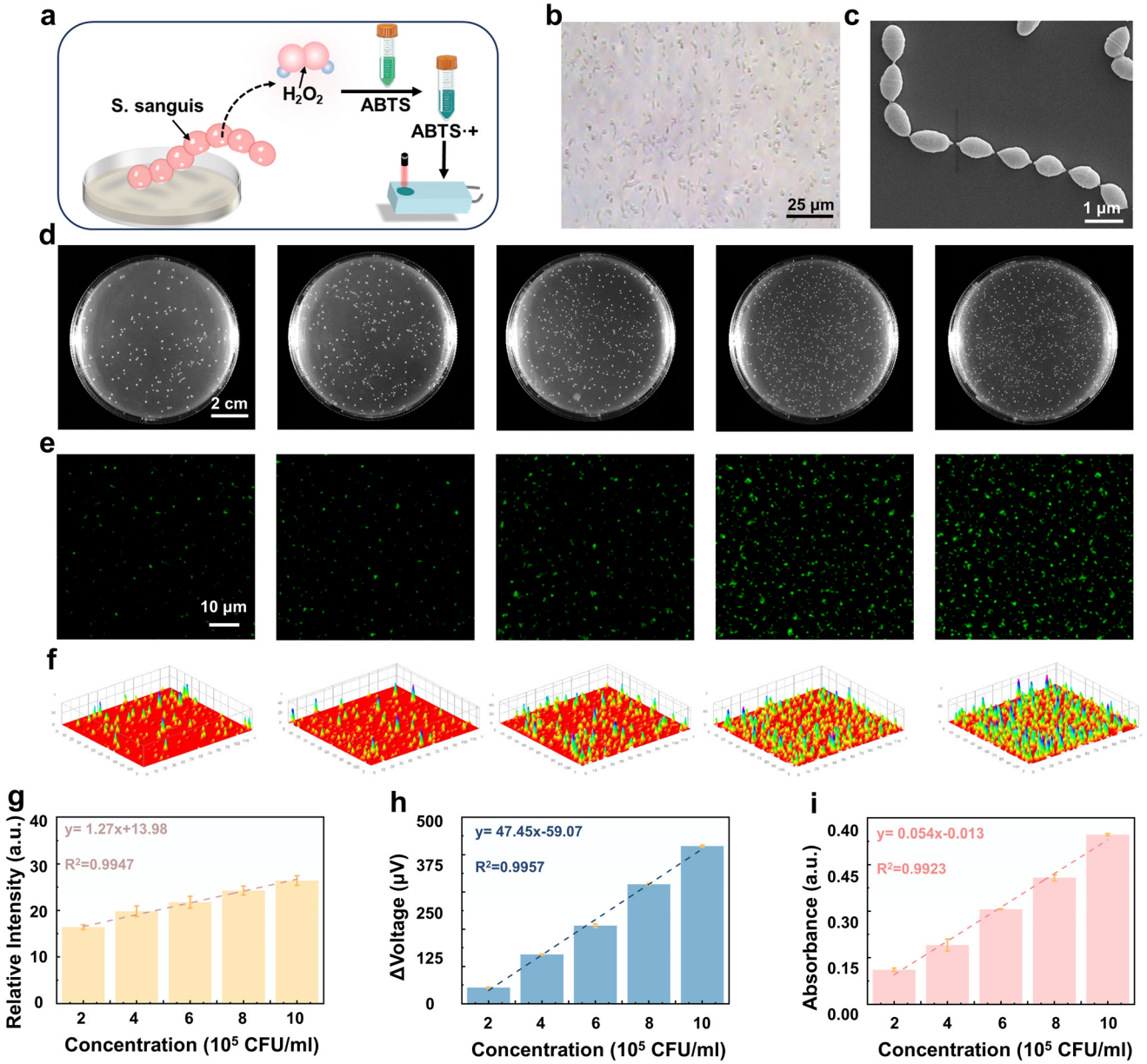

Fig. 5 (a) Schematic diagram for the detection of *S. sanguinis*. (b) Microscopy image of *S. sanguinis*. (c) Scanning electron microscopy image of *S. sanguinis*. (d) Plate images of *S. sanguinis* at different concentrations. (e) Reactive oxygen species (ROS) fluorescence intensity and 3D plot (f) of *S. sanguinis* at different concentrations. (g) Average fluorescence intensity of *S. sanguinis* at different concentrations. (h) Ag_2Se-based biosensor testing of *S. sanguinis* at different concentrations. (i) Kit testing of *S. sanguinis* at different concentrations.

colonies on the medium increased sequentially, showing a direct correlation with the concentration of *S. sanguinis* (Fig. 5d). To investigate the relationship between productive H_2O_2 and concentrations of *S. sanguinis*, *S. sanguinis* at different concentrations were incubated in an anaerobic environment and then stained using a ROS assay kit (Fig. 5e). The results indicated that fluorescence intensity increased with the rise in the bacterial concentration. The heat map revealed that the higher the concentration, the higher the total fluorescence intensity of ROS (Fig. 5f). Additionally, the

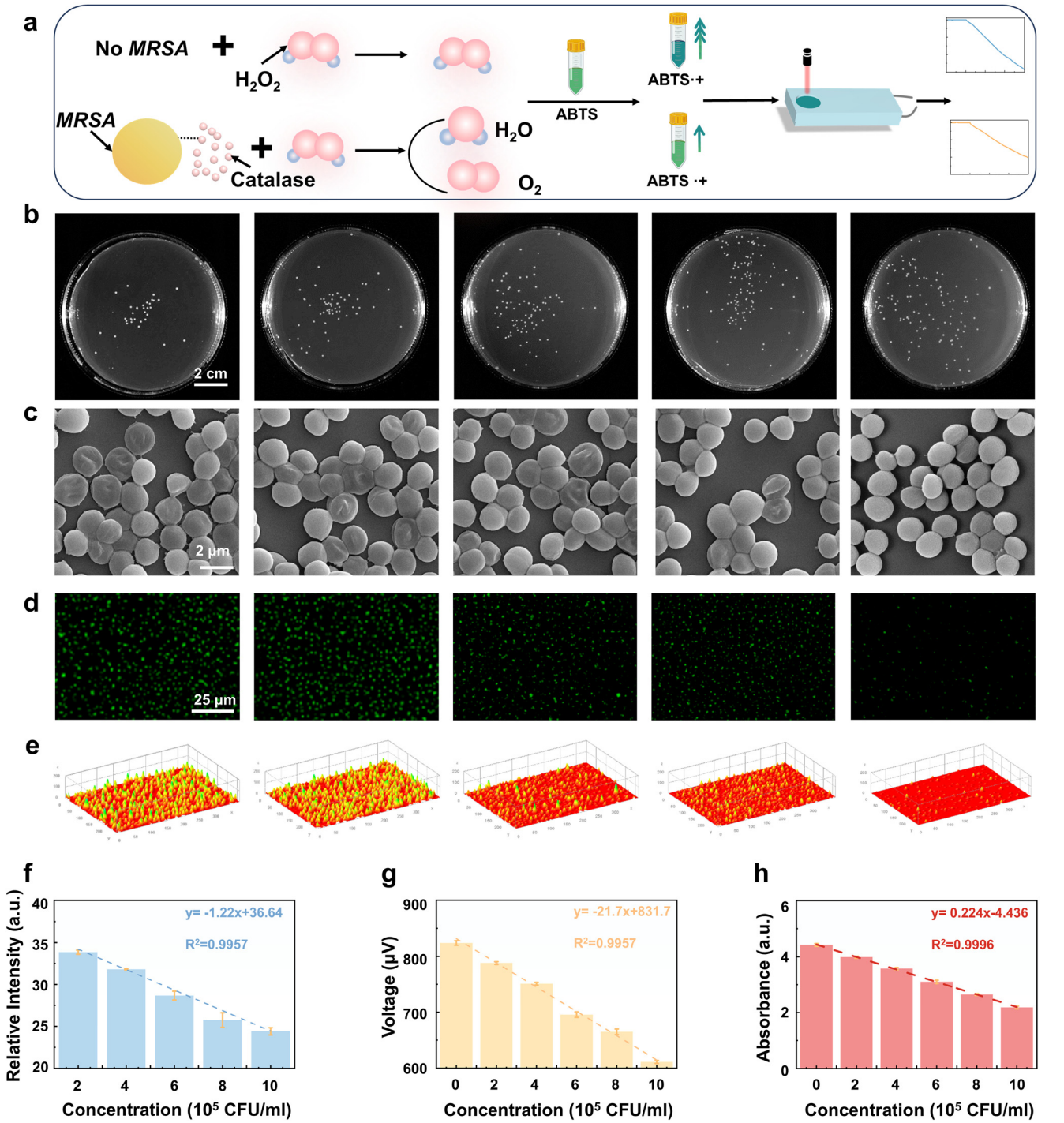

Fig. 6 (a) Schematic diagram of the steps and principles for detecting *MRSA* using sensors, (b) plate images of *MRSA* at different concentrations, (c) microscopic morphology under scanning electron microscopy after incubating *MRSA* at different concentrations with 10 μM H_2O_2, and reactive oxygen species (ROS) fluorescence intensity (d) and its 3D plot (e), as well as (f) average fluorescence intensity. (g) Sensor and kit test results (h) of the supernatant after incubation.

average intensity per unit area increased with increasing concentration, showing a linear relationship (Fig. 5g). Following this, varying concentrations of *S. sanguinis* in PBS were subjected to anaerobic incubation and subsequent centrifugation. The resulting supernatants were then analyzed for H_2O_2 concentration using the Ag_2Se-based biosensor. The biosensor readings exhibited a direct linear correlation with the *S. sanguinis* concentrations (Fig. 5h). In parallel, an H_2O_2 assay kit was employed to quantify the H_2O_2 levels in the supernatants, which aligned with the trends detected by our biosensor (Fig. 5i), further validating the reliability of the Ag_2Se-based sensor. Consequently, the LOD of the biosensor for *S. sanguinis* can be determined as 3.1×10^4 CFU ml^{-1}. To validate the specificity of our detection approach, we performed a comparative study (Fig. S13†), assessing the response of the Ag_2Se-based biosensor to *S. sanguinis* as well as a variety of common substances such as PBS, glucose, sodium chloride, and cellular components. The data demonstrated that the biosensor selectively responded to H_2O_2, confirming its specificity for this target. Therefore, this sensor is of great significance for detecting *S. sanguinis* and further guiding the diagnosis and treatment of diseases such as dental caries or endocarditis.

2.6. Biosensor-based detection of *MRSA*

As a type of Gram-positive bacteria, *MRSA* exhibits resistance to most commonly used antibiotics, leading to a range of problems that span from mild skin infections to severe, life-threatening conditions such as pneumonia, bacteremia, endocarditis, necrotizing fasciitis, and bone infections.[51,52] Consequently, the Ag_2Se-based biosensor is designed to utilize its sensitive detection mechanisms to accurately detect *MRSA*, enhancing diagnostic precision in clinical and sensor technology applications. *MRSA* can secrete catalase to resist the damage of H_2O_2 by decomposing it into H_2O and oxygen.[53] As displayed in Fig. 6a, *MRSA* is endowed with the capability to decompose H_2O_2. Following exposure to a range of *MRSA* concentrations in a 10 μM H_2O_2 solution and an intervening incubation period, the supernatant collected after centrifugal separation is then subjected to further incubation with a reference solution. The decomposition of H_2O_2 caused by the presence of bacteria leads to diminished production of $ABTS^{\bullet+}$, leading to a reduced temperature gradient and a diminished electrical signal from the Ag_2Se-based biosensor. The concentration of *MRSA* is determined by comparing the weakened electrical signal with the original H_2O_2 signal. *MRSA* at various concentrations was cultured on LB agar, as shown in Fig. 6b. After one day of incubation, the colonies on agar showed a positive correlation with the concentration. The microscopic morphologies of *MRSA* at different concentrations after incubation with the same concentration (10 μM) of H_2O_2 are shown in Fig. 6c. The results indicated that with an elevation in *MRSA* concentration, there was a marked decrease in the proportion of wrinkled cells, signifying a diminished impact of H_2O_2-induced damage, suggesting that the catalase secreted by *MRSA* has a protective effect. This investigation conducted reactive oxygen species (ROS) staining on *MRSA* samples exposed to a consistent concentration of 10 μM H_2O_2, revealing a noteworthy inverse correlation. Notably, the sample containing the least concentration of *MRSA* demonstrated the highest ROS fluorescence intensity, as depicted in Fig. 6d. A 3D fluorescence intensity plot, depicted in Fig. 6e, offers a clearer perspective on this trend, showing a decline in ROS intensity with increasing *MRSA* concentrations. The mean fluorescence intensity data quantified in Fig. 6f supports this finding, showing that higher bacterial concentrations lead to a more marked reduction in H_2O_2 levels. Utilizing an Ag_2Se-based biosensor to assay the supernatant from H_2O_2-incubated *MRSA* following centrifugation, we noted a decrease in voltage signals with rising *MRSA* concentrations, implying that H_2O_2 was being decomposed by the catalase enzyme released by *MRSA*, as depicted in Fig. 6g. The linear relationship between the voltage signal and the bacterial concentration demonstrates the potential of the Ag_2Se-based sensor for *MRSA* detection. After testing the supernatant with a commercially available H_2O_2 assay kit, the results showed a similar trend, further enhancing the reliability of the sensor (Fig. 6h). The sensor demonstrates a detection threshold of 6×10^4 CFU ml^{-1} for *MRSA*, exceeding the microbial concentration necessary for clinical diagnosis of an infection. This sensitivity positions the TE sensor as a promising tool for *MRSA* detection and holds significance for identifying various drug-resistant infectious diseases. The specificity for *MRSA* was also verified, and the results indicated that the sensor exhibited effective specificity toward *MRSA* (Fig. S13†). Compared to other TE materials such as Bi_2Te_3 and PEDOT:PSS, Ag_2Se-based biosensors exhibit a faster response time, are reusable, and can detect bacteria (Table S2†). This study proposes an innovative TE approach for the detection of bacteria including *S. sanguinis* and *MRSA*. Despite the method's potential, its clinical application is beset with challenges. Moving forward, the conjunction of this technique with antibody conjugation or fluorescence technologies may represent a pivotal step in surmounting these obstacles within the biosensor domain.

3. Conclusion

In this study, we have successfully fabricated a TE material-based sensory system capable of quantifying H_2O_2 concentrations across a wide dynamic range, from 0.26 μM to 10.0 μM. In the fabrication of the sensor device, Ag_2Se nanofilms were deposited onto 3D-printed resin substrates through ion sputtering with the aid of masks, serving as the sensing element. The sensor device can detect energy fluctuations resulting from photothermal–electric conversion, which is induced by photothermal agents that respond to variations in the H_2O_2 concentration. Subsequently, the practical application of the sensory device was tested through its performance in bacterial detection and the evaluation of H_2O_2 concentration in beverages. Significantly, the sensor achieved a detection threshold as low as 10^4 CFU ml^{-1} for bacterial concen-

trations, surpassing the existing clinical diagnostic standards. This high sensitivity holds promise for the accurate diagnosis of periodontitis and the identification of drug-resistant bacterial infections. The TE sensory strategy presented in this study holds promise for detecting biomarkers. It offers a simple, rapid, and cost-effective reproducible solution, making it suitable for application in medical diagnostics, personalized health monitoring, and verifying food safety.

Author contributions

Huangshui Ma: writing – original draft, methodology, and investigation. Shiyu Pu: writing – review & editing, methodology, and investigation. Shiyu Jia: writing – review & editing and formal analysis. Shengduo Xu: writing – review & editing and formal analysis. Qiwei Yu: writing – review & editing and formal analysis. Lei Yang: writing – writing – review & editing and supervision. Hao Wu: writing – review & editing and supervision. Qiang Sun: writing – review & editing, supervision, methodology, and funding acquisition.

Data availability

The data that support the findings of this study are available from the corresponding author upon reasonable request.

Conflicts of interest

The authors declare no competing financial interest.

Acknowledgements

This work was supported by the Sichuan Science and Technology Program (Grant No. 2023YFG0220, 2023ZYD0064, and 2024YFHZ0309) and the Fundamental Research Funds for the Central Universities and Research Funding from West China School/Hospital of Stomatology Sichuan University, No. QDJF2022-2.

References

1 J. Wu, H. Liu, W. Chen, B. Ma and H. Ju, *Nat. Rev. Bioeng.*, 2023, **1**, 346–360.
2 A. Minopoli, B. Della Ventura, B. Lenyk, F. Gentile, J. A. Tanner, A. Offenhäusser, D. Mayer and R. Velotta, *Nat. Commun.*, 2020, **11**, 6134.
3 H.-J. Chang, A. Zúñiga, I. Conejero, P. L. Voyvodic, J. Gracy, E. Fajardo-Ruiz, M. Cohen-Gonsaud, G. Cambray, G.-P. Pageaux, M. Meszaros, L. Meunier and J. Bonnet, *Nat. Commun.*, 2021, **12**, 5216.
4 X. Mu, T. D. Evans and F. Zhang, *Nat. Commun.*, 2024, **15**, 5299.
5 P. Zhao, W. Xue, Y. Zhang, S. Zhi, X. Ma, J. Qiu, T. Zhang, S. Ye, H. Mu, J. Cheng, X. Wang, S. Hou, L. Zhao, G. Xie, F. Cao, X. Liu, J. Mao, Y. Fu, Y. Wang and Q. Zhang, *Nature*, 2024, **631**, 777–782.
6 D. Wang, J. Ding, Y. Ma, C. Xu, Z. Li, X. Zhang, Y. Zhao, Y. Zhao, Y. Di, L. Liu, X. Dai, Y. Zou, B. Kim, F. Zhang, Z. Liu, I. McCulloch, M. Lee, C. Chang, X. Yang, D. Wang, D. Zhang, L.-D. Zhao, C.-a. Di and D. Zhu, *Nature*, 2024, **632**, 528–535.
7 W. He, D. Wang, H. Wu, Y. Xiao, Y. Zhang, D. He, Y. Feng, Y.-J. Hao, J.-F. Dong, R. Chetty, L. Hao, D. Chen, J. Qin, Q. Yang, X. Li, J.-M. Song, Y. Zhu, W. Xu, C. Niu, X. Li, G. Wang, C. Liu, M. Ohta, S. J. Pennycook, J. He, J.-F. Li and L.-D. Zhao, *Science*, 2019, **365**, 1418–1424.
8 W. Zhao, Z. Liu, P. Wei, Q. Zhang, W. Zhu, X. Su, X. Tang, J. Yang, Y. Liu, J. Shi, Y. Chao, S. Lin and Y. Pei, *Nat. Nanotechnol.*, 2017, **12**, 55–60.
9 X.-L. Shi, J. Zou and Z.-G. Chen, *Chem. Rev.*, 2020, **120**, 7399–7515.
10 H. Yu, Z. Hu, J. He, Y. Ran, Y. Zhao, Z. Yu and K. Tai, *Nat. Commun.*, 2024, **15**, 2521.
11 H. Ma, S. Pu, H. Wu, S. Jia, J. Zhou, H. Wang, W. Ma, Z. Wang, L. Yang and Q. Sun, *ACS Appl. Mater. Interfaces*, 2024, **16**, 7453–7462.
12 R. Li, W. Ou, J. Zhu, Q. Deng, X. Tan, Q. Zhao, T. Lu, S. Gao, H. Ma, H. Wu, Q. Sun and R. Ang, *Chem. Eng. J.*, 2024, **497**, 154624.
13 J. Zhu, X. Tan, M. Hong, Y. Wei, H. Ma, F. Feng, Y. Luo, H. Wu, Q. Sun and R. Ang, *Adv. Energy Mater.*, 2024, **14**, 2402552.
14 D. Yang, X.-L. Shi, M. Li, M. Nisar, A. Mansoor, S. Chen, Y. Chen, F. Li, H. Ma, G. X. Liang, X. Zhang, W. Liu, P. Fan, Z. Zheng and Z.-G. Chen, *Nat. Commun.*, 2024, **15**, 923.
15 Y. Liu, Q. Zhang, A. Huang, K. Zhang, S. Wan, H. Chen, Y. Fu, W. Zuo, Y. Wang, X. Cao, L. Wang, U. Lemmer and W. Jiang, *Nat. Commun.*, 2024, **15**, 2141.
16 Y. Liu, X. Wang, S. Hou, Z. Wu, J. Wang, J. Mao, Q. Zhang, Z. Liu and F. Cao, *Nat. Commun.*, 2023, **14**, 3058.
17 Q.-X. Hu, W.-D. Liu, L. Zhang, H. Gao, D.-Z. Wang, T. Wu, X.-L. Shi, M. Li, Q.-F. Liu, Y.-L. Yang and Z.-G. Chen, *Adv. Energy Mater.*, 2024, **14**, 2401890.
18 Y. Lu, Y. Zhou, W. Wang, M. Hu, X. Huang, D. Mao, S. Huang, L. Xie, P. Lin, B. Jiang, B. Zhu, J. Feng, J. Shi, Q. Lou, Y. Huang, J. Yang, J. Li, G. Li and J. He, *Nat. Nanotechnol.*, 2023, **18**, 1281–1288.
19 Z. Zhou, Y. Huang, B. Wei, Y. Yang, D. Yu, Y. Zheng, D. He, W. Zhang, M. Zou, J.-L. Lan, J. He, C.-W. Nan and Y.-H. Lin, *Nat. Commun.*, 2023, **14**, 2410.
20 B. Tian, H. Ma, X. An, Y. Mao, Q. Deng, Q. Sun and R. Ang, *Device*, 2024, **2**, 100524.
21 A. Moin, A. Zhou, A. Rahimi, A. Menon, S. Benatti, G. Alexandrov, S. Tamakloe, J. Ting, N. Yamamoto, Y. Khan, F. Burghardt, L. Benini, A. C. Arias and J. M. Rabaey, *Nat. Electron.*, 2021, **4**, 54–63.
22 P. Rai, M. Parrish, I. J. J. Tay, N. Li, S. Ackerman, F. He, J. Kwang, V. T. Chow and B. P. Engelward, *Proc. Natl. Acad. Sci. U. S. A.*, 2015, **112**, E3421–E3430.

23 C. Nathan and A. Cunningham-Bussel, *Nat. Rev. Immunol.*, 2013, **13**, 349–361.
24 J. E. Giaretta, H. Duan, F. Oveissi, S. Farajikhah, F. Dehghani and S. Naficy, *ACS Appl. Mater. Interfaces*, 2022, **14**, 20491–20505.
25 B. E. Watt, A. T. Proudfoot and J. A. Vale, *Toxicol. Rev.*, 2004, **23**, 51–57.
26 L. Zheng, Z. Chen, A. Itzek, M. Ashby and J. Kreth, *J. Bacteriol.*, 2011, **193**, 516–526.
27 B. R. Singh, B. N. Singh, W. Khan, H. B. Singh and A. H. Naqvi, *Biomaterials*, 2012, **33**, 5753–5767.
28 K. Wu, X. Wu, M. Chen, H. Wu, Y. Jiao and C. Zhou, *Chem. Eng. J.*, 2020, **387**, 124127.
29 X. Chen, X. Ren, L. Zhang, Z. Liu and Z. Hai, *Anal. Chem.*, 2020, **92**, 14244–14250.
30 A. S. Ivanova, A. D. Merkuleva, S. V. Andreev and K. A. Sakharov, *Food Chem.*, 2019, **283**, 431–436.
31 C.-L. Shen, Q. Lou, J.-H. Zang, K.-K. Liu, S.-N. Qu, L. Dong and C.-X. Shan, *Adv. Sci.*, 2020, **7**, 1903525.
32 K. Wang, Y. Sun, W. Xu, W. Zhang, F. Zhang, Y. Qi, Y. Zhang, Q. Zhou, B. Dong, C. Li, L. Wang and L. Xu, *Sens. Actuators, B*, 2022, **355**, 131298.
33 Y. Wu, P. Balasubramanian, Z. Wang, J. A. S. Coelho, M. Prslja, R. Siebert, M. B. Plenio, F. Jelezko and T. Weil, *J. Am. Chem. Soc.*, 2022, **144**, 12642–12651.
34 M. P. Murphy, H. Bayir, V. Belousov, C. J. Chang, K. J. A. Davies, M. J. Davies, T. P. Dick, T. Finkel, H. J. Forman, Y. Janssen-Heininger, D. Gems, V. E. Kagan, B. Kalyanaraman, N.-G. Larsson, G. L. Milne, T. Nyström, H. E. Poulsen, R. Radi, H. Van Remmen, P. T. Schumacker, P. J. Thornalley, S. Toyokuni, C. C. Winterbourn, H. Yin and B. Halliwell, *Nat. Metab.*, 2022, **4**, 651–662.
35 C. Hao, X. Wu, M. Sun, H. Zhang, A. Yuan, L. Xu, C. Xu and H. Kuang, *J. Am. Chem. Soc.*, 2019, **141**, 19373–19378.
36 J. Chen, Q. Sun, D. Bao, B.-Z. Tian, Z. Wang, J. Tang, D. Zhou, L. Yang and Z.-G. Chen, *Acta Mater.*, 2021, **220**, 117335.
37 Y.-Y. Liao, Q. Sun, X.-P. Jiang, H. Wu, B.-Z. Tian, Z.-G. Wang, K. Zheng and L. Yang, *J. Mater. Sci. Technol.*, 2024, **179**, 138–144.
38 M. Gao, Y. Luo, W. Li, L. Zheng and Y. Pei, *J. Mater. Chem. B*, 2024, **12**, 6847–6855.
39 J. Wu, Q. Yang, Q. Li, H. Li and F. Li, *Anal. Chem.*, 2021, **93**, 4084–4091.
40 N. Nasirizadeh, Z. Shekari, A. Nazari and M. Tabatabaee, *J. Food Drug. Anal.*, 2016, **24**, 72–82.
41 N. Mohd Nasir, B. K. Lee, S. S. Yap, K. L. Thong and S. L. Yap, *Arch. Biochem. Biophys.*, 2016, **605**, 76–85.
42 F. Jiang, C. Lin, J. Cheng, H. Yu, Y. Zhou, X. Ma, L. Wu, S. Ye, J. Chen, S. Zhi, Y. Xu, P. Zhao, X. Wang, F. Cao, Q. Zhang and J. Mao, *Adv. Funct. Mater.*, 2024, 2415000.
43 R. Venkatasubramanian, E. Siivola, T. Colpitts and B. O'Quinn, *Nature*, 2001, **413**, 597–602.
44 S. Sen and R. Chakraborty, in *Exploring the Nutrition and Health Benefits of Functional Foods*, ed. H. U. Shekhar, Z. H. Howlader and Y. Kabir, IGI Global, Hershey, PA, USA, 2017, pp. 265–300, DOI: **10.4018/978-1-5225-0591-4.ch013**.
45 X. Chen, D. He, J. Shentu, S. Yang, Y. Yang, Y. Wang, R. Zhang, K. Wang, J. Qian and L. Long, *Chem. Eng. J.*, 2023, **472**, 144900.
46 R. López, P. C. Smith, G. Göstemeyer and F. Schwendicke, *J. Clin. Periodontol.*, 2017, **44**, S145–S152.
47 N. B. Pitts, D. T. Zero, P. D. Marsh, K. Ekstrand, J. A. Weintraub, F. Ramos-Gomez, J. Tagami, S. Twetman, G. Tsakos and A. Ismail, *Nat. Rev. Dis. Primers*, 2017, **3**, 17030.
48 R. A. Giacaman, S. Torres, Y. Gómez, C. Muñoz-Sandoval and J. Kreth, *Arch. Oral Biol.*, 2015, **60**, 154–159.
49 L. Zhu and J. Kreth, *Oxid. Med. Cell. Longevity*, 2012, **2012**, 717843.
50 L. Zhu, Y. Zhang, J. Fan, M. C. Herzberg and J. Kreth, *Mol. Oral Microbiol.*, 2011, **26**, 117–126.
51 H. Ge, Y. Wang and X. Zhao, *Microb. Pathog.*, 2022, **162**, 105306.
52 J. Xie, M. Zhou, Y. Qian, Z. Cong, S. Chen, W. Zhang, W. Jiang, C. Dai, N. Shao, Z. Ji, J. Zou, X. Xiao, L. Liu, M. Chen, J. Li and R. Liu, *Nat. Commun.*, 2021, **12**, 5898.
53 Y. Imai, K. J. Meyer, A. Iinishi, Q. Favre-Godal, R. Green, S. Manuse, M. Caboni, M. Mori, S. Niles, M. Ghiglieri, C. Honrao, X. Ma, J. J. Guo, A. Makriyannis, L. Linares-Otoya, N. Böhringer, Z. G. Wuisan, H. Kaur, R. Wu, A. Mateus, A. Typas, M. M. Savitski, J. L. Espinoza, A. O'Rourke, K. E. Nelson, S. Hiller, N. Noinaj, T. F. Schäberle, A. D'Onofrio and K. Lewis, *Nature*, 2019, **576**, 459–464.